

Search for continuous gravitational waves from PSR J0437–4715 with a hidden Markov model in O3 LIGO data

Andres F. Vargas^{1,2,*} and Andrew Melatos^{1,2}

¹*School of Physics, University of Melbourne, Parkville, Vic, 3010, Australia*

²*OzGrav-Melbourne, Australian Research Council Centre of Excellence for Gravitational Wave Discovery, Parkville, Victoria, 3010, Australia*

(Dated: August 9, 2022)

Results are presented for a semi-coherent search for continuous gravitational waves from the millisecond pulsar PSR J0437–4715, using a hidden Markov model to track spin wandering, in LIGO data from the third LIGO-Virgo observing run. This is the first search for PSR J0437–4715 to cover a wide frequency range from 60 Hz to 500 Hz and simultaneously accommodate random spin deviations from the secular radio ephemeris. Two searches are performed with plausible coherence times of 10 days and 30 days, as the frequency wandering time-scale of the gravitational-wave-emitting quadrupole is unknown. The former analysis yields no surviving candidates, while the latter yields five candidates after the veto procedure. The detection statistic of each of the five survivors is mapped as a function of sky position, in preparation for follow-up analyses in the future, e.g. during LIGO-Virgo-KAGRA fourth observing run.

I. INTRODUCTION

Rapidly rotating neutron stars (NSs) are potential sources of continuous gravitational waves (GWs) detectable by terrestrial detectors such as the Advanced Laser Interferometer Gravitational-wave Observatory (LIGO) [1–4], Advanced Virgo [5], and the Kamioka Gravitational Wave Detector (KAGRA) [6]. Several mechanisms, such as elastic stresses [7, 8], magnetic gradients [9–11], r -modes [12–14], or non-axisymmetric circulation of the superfluid interior [15–18], can produce an oscillating quadrupole moment which emits continuous GWs at specific multiples of the NS spin frequency f_* [1].

Millisecond pulsars (MSPs) with an accurately measured radio ephemeris, such as PSR J0437–4715 [19, 20], are key targets for continuous GWs searches. Non-axisymmetries, supported elastically or magnetically, can be generated in the NS crust through accretion [7, 21, 22] and subside with age [23]. In addition, the r -mode instability may play a role in the spin history of these objects [24–26], with periods of activity ranging from short [27] to long [28] timescales. These different avenues for MSPs to maintain an oscillating quadrupole moment have served historically to motivate coherent searches for continuous GWs, using a bar detector [29] or terrestrial interferometers [30–32].

In this paper we search for PSR J0437–4715 with a hidden Markov model (HMM) algorithm, which tracks spin wandering [33–37]. There are strong astrophysical motivations to target this object. (1) It is nearby, at a distance $D = 156.3 \pm 1.3$ pc measured from parallax to 1% precision [38], and the GW strain scales $\propto D^{-1}$. (2) It spins rapidly, with $f_* = 173.69$ Hz [19], and the GW strain scales $\propto f_*^2$. (3) Radiation at f_* and $2f_*$ from a

static mountain and $\approx 4f_*/3$ [39] from an r -mode falls in a sensitive band of the LIGO detectors, separated from instrumental noise lines [40]. (4) The orbital elements are known to high accuracy from radio pulsar timing, e.g. the orbital period $P = 5.741$ days has an uncertainty of $\sigma_P = 3 \times 10^{-7}$ days (one standard deviation) [41].

Previous searches for PSR J0437–4715, like [30–32], are confined to narrow ranges of ~ 1 Hz around f_* , and $2f_*$. It is eminently possible that the GW-emitting quadrupole is not locked to the crust, so that the GW signal frequency is displaced significantly from simple rational multiples of f_* and possibly also wanders stochastically with time [42]. The HMM algorithm is adept at tracking a displaced and wandering tone. Hitherto, HMM narrow-band searches run in sub-bands of ~ 1 Hz around multiples of the spin frequency like f_* and $2f_*$ (mountains) and $4f_*/3$ (r -modes) [43–45]. However, the HMM runs so fast (~ 1 day), when the orbital elements are known accurately as for PSR J0437–4715, that we elect to cover all options in this paper and search LIGO’s most sensitive frequency band from 60 Hz to 500 Hz, to ensure that nothing is missed. This strategy acknowledges recent theoretical work that r -modes may emit far from $4f_*/3$ [39, 46].

The paper is organized as follows. Section II introduces the HMM scheme, and the frequency domain matched filter, i.e. the \mathcal{J} -statistic, used for the search. Section III briefly describes the target and its parameter space. In Section IV the search pipeline and threshold procedure are reviewed. Section V presents the search results. Astrophysical implications are canvassed briefly in Section VI.

II. HMM ALGORITHM

The HMM analysis pipeline involves two components. The first, namely the HMM itself, tracks the frequency

* afvargas@student.unimelb.edu.au

evolution of the signal from one time-step to the next. It is described in Section II A. The second, namely the \mathcal{J} -statistic, computes the likelihood that a signal (if any) is present in the data between two time-steps as a function of the frequency. It is described in Section II B.

A. Formalism

A HMM is characterized by a hidden state variable, $q(t)$, and an observable state variable, $o(t)$. As in previous works [33–37] the hidden state variable is the GW frequency $f(t)$. One can have $f(t) \neq f_*(t)$ because (i) different emission mechanisms produce GWs at different multiples of $f_*(t)$ [1]; (ii) the GW-emitting quadrupole may not corotate exactly with the stellar surface and magnetosphere, whence the electromagnetic emission originates; and (iii) $f(t)$ and $f_*(t)$ may wander stochastically in response to fluctuating internal torques [42], such that the lag $f(t) - f_* \neq 0$ fluctuates as well.

The HMM jumps between discrete hidden state values $\{q_1, \dots, q_{N_Q}\}$ at discrete epochs $\{t_0, \dots, t_{N_T}\}$. The probability to jump from q_i at t_n to q_j at t_{n+1} is given by the transition matrix $A_{q_j q_i}$, which takes the form

$$A_{q_j q_i} = \frac{1}{3} (\delta_{q_j q_{i-1}} + \delta_{q_j q_i} + \delta_{q_j q_{i+1}}), \quad (1)$$

where δ_{ij} is the Kronecker delta. Eq. (1) describes a piece-wise constant signal model, where $f(t)$ jumps by 0, or ± 1 frequency bins with equal probability at each epoch. Other signal models are viable too, of course, but tests on synthetic data verify that the performance of the HMM depends weakly on the exact form of $A_{q_j q_i}$ [33, 47].

The Fourier transform of the time-domain data collected by the detectors is used as the observable state variable. The complete data stream, with duration T_{obs} , is divided into N_T segments of duration T_{drift} , following $N_T = \text{floor}(T_{\text{obs}}/T_{\text{drift}})$. The coherence time T_{drift} is chosen judiciously to avoid $f(t)$ wandering more than one frequency bin per time-step. In general HMM searches [34–37] use the observed X-ray flux variability of systems like Scorpius X-1 to infer the stochastic variation in $f(t)$ [42, 48] and make an informed choice of T_{drift} . Section IV expands on the choice of T_{drift} for this search. The likelihood of observing o_j if the hidden state variable is q_i is encoded in the emission probability matrix $L_{o_j q_i}$. We use the \mathcal{J} -statistic, a frequency domain estimator reviewed in Section II A, to calculate $L_{o_j q_i}$ [35].

The probability the hidden state variable follows a path $Q = \{q(t_1), \dots, q(t_{N_T})\}$, given the observations $O = \{o(t_0), \dots, o(t_{N_T})\}$, is the product of the transition and emission probabilities per time-step, namely

$$\Pr(Q|O) = L_{o(t_{N_T})q(t_{N_T})} A_{q(t_{N_T})q(t_{N_T-1})} \times \dots \times L_{o(t_1)q(t_1)} A_{q(t_1)q(t_0)} \Pi_{q(t_0)}, \quad (2)$$

where $\Pi_{q(t_0)}$ is the prior probability of starting at $q(t_0)$ and is taken to be uniform across all initial states, with $\Pi_{q(t_0)} = 1/N_Q$.

The Viterbi algorithm searches efficiently for the path Q^* that maximizes Eq. (2) [49]. A thorough explanation of the algorithm, in the context of GW searches, is included in Appendix A of Ref. [34]. As a detection statistic we use the log likelihood of the most likely path given the data, i.e. $\mathcal{L} = \ln \Pr(Q^*|O)$.

B. \mathcal{J} -statistic

The emission probability $L_{o(t_n)q(t_n)}$ relates the observed data between two consecutive epochs, $\{o(t')|t_n \leq t' \leq t_n + T_{\text{drift}}\}$, to the hidden states occupied at the first epoch, $q(t_n)$. $L_{o(t_n)q(t_n)}$ is expressed in terms of the \mathcal{J} -statistic [35, 36]. The \mathcal{J} -statistic extends the traditional \mathcal{F} -statistic [50], a matched filter for a biaxial rotor [51], by tracking the movement of the NS in its binary system and accommodating the orbital Doppler shift of the GW carrier frequency. To track the NS, the \mathcal{J} -statistic assumes a circular Keplerian orbit (PSR J0437–4715 has orbital eccentricity $e = 1.9180 \times 10^{-5}$ [52]). It is a function of three binary orbital parameters: the orbital period P , the orbital phase at a reference time ϕ_a , and the projected semi-major axis a_0 .

The \mathcal{J} -statistic is efficient computationally. It executes on graphical processing units (GPU) and ingests prefabricated \mathcal{F} -statistic *atoms* [53] which are independent of the binary orbital parameters. The complete definition of the \mathcal{J} -statistic can be found in Section III in Ref. [35].

III. PSR J0437–4715

PSR J0437–4715, discovered in 1993 [19], is the brightest nearby millisecond pulsar known. It exists in a binary with a cool hydrogen atmosphere white dwarf [54] and travels at $104.71 \pm 0.95 \text{ km s}^{-1}$ [38] through the interstellar medium. As well as the radio ephemeris, the study of this system spans the optical [55], X-ray [56], and ultraviolet [57] bands, which translates into accurate electromagnetic values for the search parameters used by the HMM pipeline. Section III A quotes the sky position and orbital parameters used throughout this paper, while Section III B justifies the frequency, and its derivatives, probed by the analysis.

A. Sky position and orbital parameters

The \mathcal{J} -statistic depends on the right ascension α and declination δ of the source (through the \mathcal{F} -statistic atoms) in addition to the three orbital parameters P , ϕ_a , and a_0 . In practice, we rewrite ϕ_a in terms of the time of passage through the ascending node, T_{asc} , via $\phi_a = 2\pi T_{\text{asc}}/P \pmod{2\pi}$. These parameters have been

measured electromagnetically at a reference epoch $T_0 = 55000$ MJD (June 18 2009) [41]. Their values and uncertainties are presented in Table I.

The electromagnetically measured value $T_{\text{asc,ref}}$, dated at T_0 , is propagated forward to the start of O3, $T_{\text{O3},0} = 1238166483$ GPS time, following

$$T_{\text{asc}} = T_{\text{asc,ref}} + N_{\text{orb}}P, \quad (3)$$

where P is the central value of the orbital period in Table I, and $N_{\text{orb}} = \text{ceil}[(T_{\text{O3},0} - T_0)/P]$ is the number of full orbits from T_0 to $T_{\text{O3},0}$. The propagated uncertainty for T_{asc} is calculated in terms of the uncertainty in the period, σ_P , as

$$\sigma_{T_{\text{asc}}} = \sqrt{\sigma_{T_{\text{asc},0}}^2 + (N_{\text{orb}}\sigma_P)^2}, \quad (4)$$

where $\sigma_{T_{\text{asc},0}}$ is the uncertainty of $T_{\text{asc,ref}}$. Eq. (4) yields $\sigma_{T_{\text{asc}}} = 55$ s. This is the value included in Table I.

Apart from T_{asc} , the remaining orbital parameters are known to high precision, with the uncertainty in P satisfying $\sigma_P \leq 10^{-1}$ s, and the uncertainty in a_0 satisfying $\sigma_{a_0} \leq 10^{-7}$ lt-s. These values and their uncertainties are obtained from the second data release of the International Pulsar Timing Array [41].

B. Spin frequency

The spin frequency is measured to high accuracy by radio timing, with $f_\star = 173.6879457375201 \pm 9 \times 10^{-13}$ Hz at T_0 . In this paper, we elect to search a much wider range of 60 Hz to 500 Hz, where LIGO is most sensitive, to account for $f(t) \neq f_\star(t)$ as discussed in Section II A. The frequency mismatch is likely to satisfy $|f(t) - \eta f_\star(t)| \ll f_\star(t)$, where η is a simple rational number (e.g. $\eta = 1, 4/3, 2$), if it is due to differential rotation between the GW-emitting quadrupole and the rigid crust [58]. However the scenario $|f(t) - \eta f_\star(t)| \sim f_\star(t)$ is also conceivable, for example if r -mode emission occurs far from $4f_\star/3$ due to complicated microphysics [39]. The HMM runs fast, so we elect to play safe and cover a wider range of eventualities in this paper by searching $60 \text{ Hz} \leq f \leq 500 \text{ Hz}$.

The search assumes $\dot{f} = 0$ throughout, e.g. when evaluating the \mathcal{J} -statistic. Table A1 in Ref. [41] quotes the measured value, $\dot{f}_\star = -1.728350 \times 10^{-15} \pm 8 \times 10^{-21}$ Hz. It causes a frequency drift $\dot{f}_\star T_{\text{obs}}$ during the observation which is 10 times smaller than one frequency bin (see Section IV A). However this target is known to possess a considerable transverse velocity $|\mathbf{v}_\perp| = 104.71 \pm 0.95 \text{ km s}^{-1}$ [38]. It is natural to ask whether corrections to \dot{f}_\star , i.e. the Shklovskii effect [59], need to be included in the analysis. We explore the effect of proper motion in the \mathcal{F} - and hence \mathcal{J} -statistics in Appendix A, while Appendix B explains how the Shklovskii effect is naturally included in

the \mathcal{F} - and hence \mathcal{J} -statistics in their existing implementations in the LIGO Scientific Collaboration Algorithm Library (LALSuite) [60]. The results in both Appendix A and Appendix B confirm that proper motion corrections are negligible for our search. As such, we approximate α and δ as constant throughout the search and persist with $\dot{f} = 0$.

IV. SEARCH IMPLEMENTATION

This section presents the practical details of the search. Section IV A justifies our selection of T_{drift} , and its implications for the search. Section IV B defines the number and spacing of the orbital parameter templates. Section IV C briefly explains the procedure to set a detection threshold in terms of a false alarm probability. Section IV D describes the data used for the search.

A. T_{drift} and frequency binning

The coherence time, T_{drift} , is a crucial component of the search as it implicitly defines the proposed signal model as described in Section II. Shorter coherence times, holding T_{obs} constant, create more segments, so that the signal is free to wander more in the same observation time. The reverse is true for longer coherence times. The frequency resolution, given by the size of the frequency bins Δf , is set by the coherence time through $\Delta f = 1/(2T_{\text{drift}})$. Using Δf and T_{drift} , the maximum absolute frequency derivative, $|\dot{f}|_{\text{max}}$, which keeps the signal within a frequency bin during a block of duration T_{drift} , is calculated as $|\dot{f}|_{\text{max}} = \Delta f/T_{\text{drift}}$.

In the absence of a GW detection from an MSP to date, there is no way to predict T_{drift} for the GW-emitting quadrupole. Instead we make a plausible estimate by analogy with the rotational irregularities observed in $f_\star(t)$ through radio timing experiments, such as timing noise [61, 62] and glitches [63]. The typical time-scale associated with deviations from the long-term secular evolution of a rotating NS is typically ~ 10 -20 days, estimated by auto-correlating pulse times of arrival [64]. This time-scale is consistent with that observed in post-glitch recoveries [16, 65–67]. In this paper we bracket the above estimates by conducting two analysis with $T_{\text{drift}}^{(i)} = 10$ days and $T_{\text{drift}}^{(ii)} = 30$ days.

The $T_{\text{drift}}^{(i)}$ -analysis matches the value used for the coherence time in previous HMM searches, allowing for direct comparisons with published results [34, 36, 37, 43, 45]. The frequency resolution is $\Delta f^{(i)} = 5.787037 \times 10^{-7}$ Hz. To assist with data handling, the search is partitioned into sub-bands. Each sub-band contains $N_f^{(i)} = 2^{20}$ frequency bins spanning a band of width $\Delta f_{\text{sub}}^{(i)} = N_f^{(i)} \Delta f^{(i)} = 0.6068148$ Hz. We choose a power of two for the number of frequency bins as this accelerates the Fourier transform in the \mathcal{J} -statistic calculation

TABLE I. Electromagnetically measured source parameters, expressed as the central value and the $1\text{-}\sigma$ uncertainty in parenthesis. All electromagnetically constrained parameter ranges are taken from Ref. [41]. The time of ascension T_{asc} stands for the value in [41] propagated to the start of O3, as described in Section III A.

Parameter	Symbol	Parameter value	Units
Right ascension	α	04 h 37 m 15.9125330(5) s	J2000
Declination	δ	$-47^\circ 15' 09'' .208600(5)$	J2000
Orbital inclination angle	ι	137.51(2)	Degrees
Projected semi-major axis	a_0	3.36672001(5)	lt-s
Orbital period	P	496 026.357(26)	s
GPS time of ascension	T_{asc}	1 265 652 972(55)	s
Spin-frequency	f_\star	173.6879457375201(9)	Hz

TABLE II. Search ranges and minimum and maximum number of grid points. All other parameters, including a_0 and P , take the central values in Table I in every template. The template ranges are the same for $T_{\text{drift}}^{(i)}$ and $T_{\text{drift}}^{(ii)}$.

Parameter	Minimum	Maximum
f / Hz	60	500
T_{asc} / s	1 265 652 809	1 265 653 136
Grid points	6	49

[35, 36]. The number of total sub-bands to consider in this analysis is $N_{\text{sub}}^{(i)} = \text{ceil} \left[(500 - 60) \text{ Hz} / \Delta f_{\text{sub}}^{(i)} \right] = 725$.

For O3 the number of contiguous segments, using $T_{\text{drift}}^{(i)}$, is $N_T^{(i)} = 36$. The maximum absolute frequency derivative, for this analysis, is $|\dot{f}^{(i)}|_{\text{max}} \approx 6.7 \times 10^{-13} \text{ Hz s}^{-1}$, which is greater than the measured long-term secular value for \dot{f}_\star in Table A1 of Ref. [41].

The $T_{\text{drift}}^{(ii)}$ -analysis uses $\Delta f^{(ii)} = 1.929012 \times 10^{-7} \text{ Hz}$, $N_f^{(ii)} = 2^{21}$, $\Delta f_{\text{sub}}^{(ii)} = 0.4045431$, and $N_{\text{sub}}^{(ii)} = 1088$ sub-bands. The number of contiguous segments, using $T_{\text{drift}}^{(ii)}$, is $N_T^{(ii)} = 12$. The maximum absolute frequency derivative consistent with $T_{\text{drift}}^{(ii)}$, $|\dot{f}^{(ii)}|_{\text{max}} \approx 7.5 \times 10^{-14} \text{ Hz s}^{-1}$, is one order of magnitude above the electromagnetically measured \dot{f}_\star [41].

For convenience, the main parameters discussed in this section are summarized in Table II.

B. Number and placing of orbital templates

We cover the orbital parameter space through a rectangular grid spanning $(a_0 \pm 3\sigma_{a_0}, T_{\text{asc}} \pm 3\sigma_{T_{\text{asc}}}, P \pm 3\sigma_P)$. The number of grid points depends on a user-selected maximum mismatch μ_{max} [68], which is the fractional loss in signal-to-noise ratio between the search using the true parameters and the search using the nearest grid point. We use $\mu_{\text{max}} = 0.1$ in this paper, following many previous analyses [34, 36, 37, 43, 45]. The number of grid points along each parameter axis is calculated using Eq. (71) of Ref. [68], viz.

$$N_{a_0} = \left\lceil 3\sqrt{2}\mu_{\text{max}}^{-1/2} f \sigma_{a_0} \right\rceil, \quad (5)$$

$$N_{T_{\text{asc}}} = \left\lceil 6\pi^2 \sqrt{2}\mu_{\text{max}}^{-1/2} f a_0 P^{-1} \sigma_{T_{\text{asc}}} \right\rceil, \quad (6)$$

$$N_P = \left\lceil \pi^2 \sqrt{6}\mu_{\text{max}}^{-1/2} f a_0 T_{\text{drift}} N_T P^{-2} \sigma_P \right\rceil. \quad (7)$$

The uncertainties in Table I, together with Eq. (5) and Eq. (7), imply $N_{a_0} = N_P = 1$ in every sub-band. As Eq. (6) depends on f , and one has $3\sigma_{T_{\text{asc}}} = 165 \text{ s}$ (see Table II), $N_{T_{\text{asc}}}$ varies for each sub-band within the range $6 \leq N_{T_{\text{asc}}} \leq 49$. In total the search covers $\sim 10^4$ templates, in stark contrast with other searches, such as O3 Scorpius X-1, for which no radio ephemeris exists, and $> 10^9$ templates are needed [37].

C. Detection threshold

The output of the HMM pipeline, for a given sub-band, is the optimal path and its associated log likelihood, $\max(\mathcal{L})$, after scanning over all possible (a_0, T_{asc}, P) triads. The reader is directed to Figure 2 of Ref. [37] for a thorough explanation of the HMM workflow.

A sub-band is flagged as containing a candidate, when $\max(\mathcal{L})$ exceeds a threshold, \mathcal{L}_{th} , consistent with a user-selected false alarm probability. We estimate the distribution of $\max(\mathcal{L})$ in pure noise, by creating synthetic Gaussian data using the `lalapp.Makefakedata.v5` program in LALSuite, the parameter values found in Table I and T_{obs} . We note this step is done for both $T_{\text{drift}}^{(i)}$ and $T_{\text{drift}}^{(ii)}$.

The false alarm probability, $\alpha_{N_{\text{tot}}}$, of a sub-band with N_{tot} log likelihoods, is a function of the false alarm probability in a single terminating frequency bin per orbital template, α , viz.

$$\alpha_{N_{\text{tot}}} = 1 - (1 - \alpha)^{N_{\text{tot}}}. \quad (8)$$

We choose to keep the number of candidates manageable for follow-up studies, and to facilitate comparison with many previous HMM searches, by setting $\alpha_{N_{\text{tot}}} = 0.01$ [34, 36, 37]. For a detailed explanation of the threshold procedure, involving simulations with Gaussian data, see Appendix A in Ref. [45].

D. O3 data

The search uses all the O3 dataset, collected by the LIGO Hanford and Livingston detectors, dated from April 1, 2019 15:00 UTC to March 27, 2020, 17:00 UTC. We do not include data from the Virgo detectors, given their lower sensitivity compared to the two LIGO observatories in the 60 Hz – 500 Hz band [69]. The O3 dataset is divided in two, namely O3a, which spans 1 April 2019 to 1 October 2019, and O3b, which spans 1 November 2019 to 26 March 2020. O3a is followed by a month-long commissioning break.

Short Fourier transforms (SFTs) are created from the “CO1 calibrated self-gated 60 Hz subtracted” dataset, which uses the procedure in Ref. [70] to remove any loud glitches and subtracts the 60 Hz noise line via the procedure described in Ref. [71]. The number of segments affected by the month-long commissioning break depends on T_{drift} . Any segment with no SFTs is replaced by a “fake” segment with uniform log likelihood across all frequency bins, to accommodate spin wandering during the commissioning break. For $T_{\text{drift}}^{(i)}$, two segments are replaced. For $T_{\text{drift}}^{(ii)}$ only one segment is replaced.

E. Vetoes

Every candidate is subjected to a hierarchy of vetoes to differentiate between non-Gaussian artifacts and astrophysical signals. In this paper, we follow previous works [34, 36, 37, 43, 45], and use the known lines veto described in Section IV E 1, and the single interferometer (IFO) veto detailed in Section IV E 2.

1. Known lines

Narrowband noise artifacts in the IFO can mimic an astrophysical signal, artificially increasing the \mathcal{F} -statistic in certain sub-bands. These noise features can be created by a multitude of causes, including the IFO suspension system or the electricity grid [40]. We veto any candidate whose optimal frequency path $f(t)$ satisfies

$$|f(t) - f_{\text{line}}| < 2\pi a_0 f_{\text{line}}/P, \quad (9)$$

for any epoch t of the search. In Eq. (9) f_{line} is the frequency of the closest noise line found in the vetted list in Ref. [72].

2. Single IFO

Astrophysical signals are likely to be weak enough to need both IFOs for detection or strong enough to appear simultaneously in both detectors, given the detectors comparable sensitivity throughout the frequency band. In contrast, the opposite is true for non-astrophysical signals caused by instrumental artifacts in an IFO.

Let $\max(\mathcal{L})_a$ and $\max(\mathcal{L})_b$, with $\max(\mathcal{L})_a > \max(\mathcal{L})_b$, denote the max log likelihoods recovered for IFO a and IFO b , separately and respectively. We use $\max(\mathcal{L})_{\cup}$ to denote the original candidate’s max log likelihood, with associated optimal path $f_{\cup}(t)$. The four possible outcomes are:

1. If one finds $\max(\mathcal{L})_a > \max(\mathcal{L})_{\cup}$ and $\max(\mathcal{L})_b < \mathcal{L}_{\text{th}}$, and the optimal path for $\max(\mathcal{L})_a$ viz. $f_a(t)$, satisfies

$$|f_{\cup}(t) - f_a(t)| < 2\pi a_0 f_{\cup}/P, \quad (10)$$

for any search epoch, then the candidate’s behaviour is consistent with an instrumental artifact in IFO a . This candidate is vetoed.

2. If one finds $\max(\mathcal{L})_a > \max(\mathcal{L})_{\cup}$ and $\max(\mathcal{L})_b < \mathcal{L}_{\text{th}}$, but Eq. (10) is not satisfied, then the candidate could be a faint astrophysical signal. The candidate is saved for post-processing.
3. If one finds $\max(\mathcal{L})_a > \mathcal{L}_{\text{th}}$ and $\max(\mathcal{L})_b > \mathcal{L}_{\text{th}}$, then the candidate could be a strong astrophysical signal, or a common noise artifact in both detectors. The candidate is saved for post-processing.
4. If one finds $\max(\mathcal{L})_a < \mathcal{L}_{\cup}$ and $\max(\mathcal{L})_b < \mathcal{L}_{\text{th}}$, then the candidate could be a weak astrophysical signal. The candidate is saved for post-processing.

V. ANALYSIS

The outputs of the search and veto procedures are presented for $T_{\text{drift}}^{(i)}$ and $T_{\text{drift}}^{(ii)}$ in Sections V A and V B respectively.

A. $T_{\text{drift}}^{(i)}$ candidates

We obtain 36 candidates with $\max(\mathcal{L}) > \mathcal{L}_{\text{th}}$. After applying the hierarchy of vetoes none of the candidates survives. The known lines veto eliminates 26 candidates, while the single IFO veto eliminates the remaining 10.

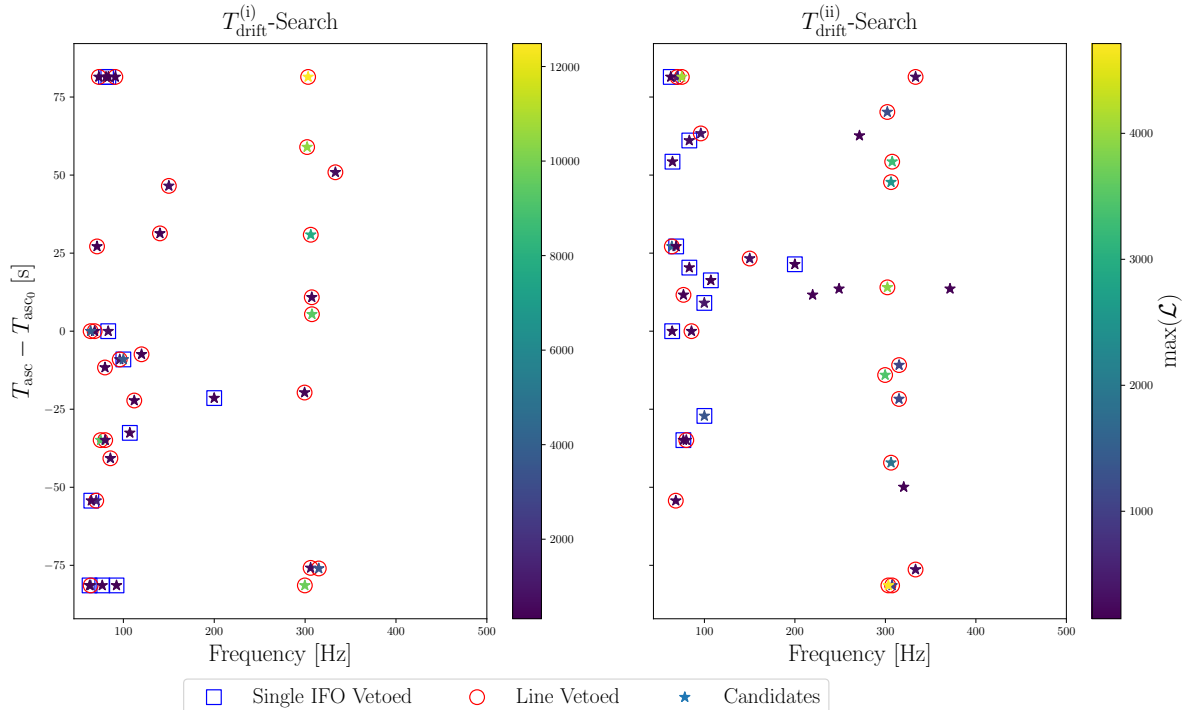


FIG. 1. Candidates (denoted by stars) plotted as a function of their frequency bin (horizontal axis) and the offset from the central time of ascension $T_{\text{asc}} - T_{\text{asc}0}$ (vertical axis), for the $T_{\text{drift}}^{(i)}$ (left panel) and the $T_{\text{drift}}^{(ii)}$ (right panel) analyses. The color scale represents $\max(\mathcal{L})$. Stars decorated with purple squares or red circles are eliminated by the single IFO or known lines veto, respectively. Undecorated stars survive both vetoes and are followed up further.

Table III summarizes the outcome of the vetoes in the 36 sub-bands containing a candidate.

The results of this analysis are plotted in the left panel of Figure 1. The vertical axis shows the offset of the candidate's T_{asc} value from the central value found in Table I (denoted as $T_{\text{asc},0}$ in Figure 1). The horizontal axis corresponds to the terminating frequency bin of the optimal path, $q^*(t_{N_T})$, of the candidate.

B. $T_{\text{drift}}^{(ii)}$ candidates

The $T_{\text{drift}}^{(ii)}$ analysis produces 37 candidates above the threshold. Out of the 37 candidates, the known lines veto eliminates 22 and the single IFO eliminates 10. All of the surviving candidates belong to outcome 4 in Section IV E 2. Table IV presents the results of the veto procedure for the candidate's sub-band. The results of the analysis are plotted in the right side panel of Figure 1. Five candidates survive the hierarchy of vetoes defined in Section IV E. Information about the surviving candidates is summarized in Table V in Appendix C. We note that the number of survivors is consistent with the expected number of false alarms, viz. $0.01 N_{\text{sub}}^{(ii)} \approx 11$.

Among the five survivors, two occur at the same value

of T_{asc} , viz. $T_{\text{asc}} = 1265652985.7228$ s. Perhaps coincidentally, the terminating frequencies of their optimal HMM paths are in the ratio $1.493 \approx 3/2$. One may seek conceivably to interpret these survivors as the first and second harmonics of a fundamental mode at ≈ 124.3 Hz, but no candidate with $\mathcal{L} > \mathcal{L}_{\text{th}}$ or known noise line [72] occurs near the latter frequency. More broadly, the frequency ratios of the five survivors are not simple fractions, as might occur with a harmonic series of instrumental or astrophysical origin.

In a similar vein, one may ask whether the frequency differences between the five survivors are simple rational multiples of an astrophysical frequency (such as f_*) or an instrumental frequency (such as a noise line). Interestingly, the first, third, fourth, and fifth survivors in Table IV are separated by integer multiples of ≈ 50 Hz, and instrumental noise lines exist at $f_{\text{line},1} = 99.88$ Hz and $f_{\text{line},2} = 150.05$ Hz which feature in the vetoes in Section IV E. Arguably, therefore, at most one (if any, and not necessarily the first) of these survivors could be astrophysical. However, it is important to note that the frequency differences between the first, third, fourth, and fifth survivors differ from simple rational multiples of $f_{\text{line},1}$ and $f_{\text{line},2}$ by up to $2\Delta f_{\text{sub}}^{(ii)} = 0.80908642$ Hz, so the pattern may be pure coincidence. The frequency differences involving the second survivor at 248.80 Hz are

TABLE III. Veto outcomes for the $T_{\text{drift}}^{(i)}$ analysis. The first column is the starting frequency of the sub-band containing the candidate. The second column is the $\max(\mathcal{L})$ of the candidate. The two last column present the results of the vetoes presented in Section IV E. \checkmark indicates the candidate survives the veto, while **X** denotes the opposite.

Sub-band (Hz)	$\max(\mathcal{L})/10^3$	Known lines veto	Single IFO veto
62.49	0.39	\checkmark	X
63.09	3.79	X	-
63.70	2.38	X	-
64.31	0.47	\checkmark	X
67.95	0.44	X	-
69.77	1.39	X	-
70.38	0.32	X	-
72.20	0.37	X	-
74.62	9.22	X	-
76.44	0.36	\checkmark	X
78.87	0.35	X	-
79.48	0.69	X	-
80.08	0.32	\checkmark	X
82.51	0.79	\checkmark	X
83.12	0.41	\checkmark	X
84.94	0.53	X	-
90.40	0.32	X	-
91.61	0.32	\checkmark	X
95.25	0.90	X	-
99.50	3.76	\checkmark	X
106.78	0.39	\checkmark	X
111.64	0.35	X	-
119.53	0.32	X	-
139.55	0.38	X	-
149.26	0.76	X	-
199.63	0.40	\checkmark	X
298.54	0.40	X	-
299.14	9.75	X	-
301.57	10.48	X	-
302.79	12.49	X	-
305.21	0.62	X	-
305.82	7.79	X	-
306.43	0.55	X	-
307.03	9.35	X	-
314.31	3.49	X	-
332.52	0.66	X	-
Total: 36			

not simple rational multiples of any obvious frequency, and the second survivor shares the same T_{asc} as the fifth survivor at 371.42 Hz. Hence one or both of the survivors at 248.80 Hz and 371.42 Hz are consistent with astrophysical or instrumental origins; all combinations remain viable without further information. The second and fifth survivors differ by $7f_*/10$ to within $\approx 1\%$.

We follow up the survivors by plotting how the detection statistic varies with the sky position of the search. We calculate \mathcal{L} for different α and δ for a uniform (α, δ) -grid covering 0.23 arcmin^2 around the source position. The aim of this test is to explore if the effective ‘‘point spread function’’ (by analogy with electromagnetic telescopes) generated by the candidate, as described through $\mathcal{L}(\alpha, \delta)$, follows the expected behaviour of an astrophysical signal [45, 73].

The results of the sky position study take the form of

sky maps such as the one displayed in Figure 2 for the survivor in the sub-band at 248.58 Hz. The sky maps for the other four survivors are presented in Appendix C. In general an astrophysical candidate’s \mathcal{L} should diminish when pointing away from the source, forming elliptical contours of constant $\mathcal{L}(\alpha, \delta)$. In Figure 2, the source location, maximum log likelihood across the map [$\max(\mathcal{L})$] and the center of the ellipse are marked by a blue, orange, and green dot, respectively. The center of the ellipse is calculated by averaging the position of pixels satisfying $\mathcal{L} > \mathcal{L}_{\text{th}}$ (marked by red dots in Figure 2). For a strong enough astrophysical signal all three locations should coincide. None of the surviving candidates display such coincidence either in Figure 2 or in Appendix C. The closest three-way coincidence is within 0.006 arcsec for the survivor at 248.58 Hz. All surviving candidates are weak, i.e. they are barely above \mathcal{L}_{th} (see Table V). This trans-

lates into small ellipses with area $\sim 207 \text{ arcsec}^2$ around each candidate, in contrast to the $\sim 4 \text{ arcmin}^2$ ellipse in Figure 6 in Ref. [45].

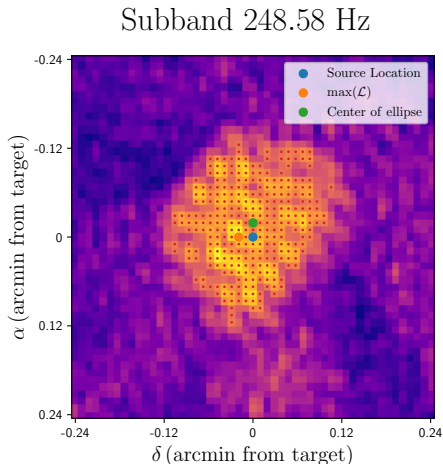


FIG. 2. Sky-map for the 248.58 Hz sub-band candidate. The source location (blue dot), maximum log likelihood location [$\max(\mathcal{L})$; orange dot], and center of the ellipse (green dot) are marked. The center of the ellipse is calculated by averaging over all pixels that satisfy $\mathcal{L} > \mathcal{L}_{\text{th}}$ (marked by red dots). In general the three dots should coincide for an astrophysical signal; here they are separated by 0.006 arcsec .

VI. CONCLUSIONS

In this paper we search for continuous GWs from PSR J0437–4715 in LIGO O3 data, using a HMM combined with the maximum-likelihood \mathcal{J} -statistic and a template grid for the time of ascension T_{asc} . As it is eminently possible to have $f(t) \neq f_{\star}(t)$, we search the band $60 \text{ Hz} \leq f \leq 500 \text{ Hz}$ to play safe and cover a range of possibilities within the most sensitive LIGO band, generalizing previous narrowband searches at simple rational multiples of f_{\star} [30–32]. As the underlying wandering time-scale of the GW-emitting quadrupole is unknown [16, 61–67], we conduct two distinct analysis with $T_{\text{drift}}^{(i)} = 10 \text{ days}$ and $T_{\text{drift}}^{(ii)} = 30 \text{ days}$. Each analysis uses a detection threshold, \mathcal{L}_{th} , with a false alarm probability of $\alpha_{N_{\text{tot}}} = 0.01$ per sub-band, set via Monte-Carlo simulations. The number of sub-bands is 725 and 1088 for the $T_{\text{drift}}^{(i)}$ and $T_{\text{drift}}^{(ii)}$ analyses, respectively.

Any sub-band with an optimal path satisfying $\max(\mathcal{L}) > \mathcal{L}_{\text{th}}$ is tested by a hierarchy of vetoes. No candidate survives the veto procedure for the $T_{\text{drift}}^{(i)}$ analysis, while five candidates survive the $T_{\text{drift}}^{(ii)}$ analysis, two of which share the same T_{asc} and are in the frequency ratio 1.493. The number of survivors is consistent with the expected number of false alarms. Sky maps of $\mathcal{L}(\alpha, \delta)$ versus search position do not reveal clear signatures of instrumental artifacts or an astrophysical origin. All five

survivors appear in sub-bands not covered by previous analyses [30–32]. We record their frequencies and orbital templates in Table V. Future searches, including during the upcoming fourth LIGO-Virgo-KAGRA observing run, will shed more light on the nature of the five survivors.

VII. ACKNOWLEDGEMENTS

This work used computational resources of the OzSTAR national facility at Swinburne University of Technology. OzSTAR is funded by Swinburne University of Technology and also the National Collaborative Research Infrastructure Strategy (NCRIS). This material is based upon work supported by NSF’s LIGO Laboratory which is a major facility fully funded by the National Science Foundation. This work has been assigned LIGO document number P2200212.

Appendix A: Proper motion in the \mathcal{F} - and \mathcal{J} -statistics

The \mathcal{F} -statistic (and hence the \mathcal{J} -statistic, which is a linear combination of \mathcal{F} -statistic values) assumes a signal model that represents a quadrupolar GW emitted by a freely precessing axisymmetric rotor [50]. The amplitude of the signal depends on the sky position of the source, i.e. α and δ , through the beam-pattern functions $F_{+}(t)$ and $F_{\times}(t)$ (as expressed in Eq. (10)-(13) in Ref. [50]). The phase of the signal, $\Psi(t)$, depends on the transverse velocity of the source projected onto the plane of the sky, \mathbf{v}_{\perp} , as expressed in Eq. (12) in Ref. [74]. The proper motion of PSR J0437–4715 is known to be significant in the context of phase-connected radio pulsar timing experiments [55, 59, 75]. It is therefore natural to ask whether it is also significant in the context of HMM GW searches, which also rely on partial phase connection; for example the \mathcal{F} - and \mathcal{J} -statistics assume phase coherence during intervals of length T_{drift} , as discussed in Section II. We explore this issue in this appendix.

The sky position of the source changes with time to leading order according to

$$\alpha(t) = \alpha + \mu_{\alpha}t, \quad (\text{A1})$$

$$\delta(t) = \delta + \mu_{\delta}t, \quad (\text{A2})$$

where α and δ are the right ascension and declination at time $t = 0$ (taken to be the values in Table I, dated T_0), and μ_{α} and μ_{δ} are the respective components of the source’s proper motion. Electromagnetically measured values for μ_{α} and μ_{δ} can be found in Table 1 of Ref. [38], namely $\mu_{\alpha} = 121.679(52) \text{ mas yr}^{-1}$, and $\mu_{\delta} = -71.820(86) \text{ mas yr}^{-1}$. Setting $t = T_{\text{obs}} = 360 \text{ days}$ in Eq. (A1) and Eq. (A2), we find the maximum angular displacement of the source from its original position is 0.12 arcsec and -0.071 arcsec in α and δ respectively.

TABLE IV. Veto outcomes for the $T_{\text{drift}}^{(\text{ii})}$ analysis, arranged as in Table III. In the last column H and L are the Hanford-only and Livingston-only $\max(\mathcal{L})$ achieved by the candidate.

Sub-band (Hz)	$\max(\mathcal{L})/10^3$	Known lines veto	Single IFO veto
62.49	0.15	✓	X
63.70	1.64	X	-
64.10	0.20	✓	X
64.51	0.19	✓	X
68.15	0.19	X	-
68.55	0.17	✓	X
69.77	0.52	X	-
74.62	4.08	X	-
76.24	0.15	✓	X
76.65	0.15	X	-
79.48	0.27	X	-
82.71	0.27	✓	X
83.12	0.18	✓	X
85.14	0.19	X	-
95.66	0.39	X	-
99.30	0.42	✓	X
99.70	1.36	✓	X
106.58	0.15	✓	X
149.46	0.34	X	-
199.63	0.16	✓	X
219.04	0.15	✓	✓; H: 120.81, L: 124.15
248.58	0.15	✓	✓; H: 124.06, L: 127.83
270.83	0.15	✓	✓; H: 120.07, L: 123.50
299.14	3.45	X	-
301.57	1.25	X	-
301.98	3.91	X	-
302.79	4.71	X	-
305.62	2.52	X	-
306.02	1.86	X	-
306.83	1.02	X	-
307.24	3.28	X	-
314.52	1.13	X	-
314.92	1.06	X	-
319.78	0.15	✓	✓; H: 123.07, L: 118.09
332.72	0.28	X	-
333.13	0.26	X	-
371.15	0.15	✓	✓; H: 123.21, L: 124.17
Total: 37			

In order to double-check that the proper motion has a negligible effect on the \mathcal{F} - and hence \mathcal{J} -statistics, we conduct the following Monte Carlo test. We generate 100 sets of synthetic data, consisting of a PSR J0437–4715-like signal plus Gaussian noise. Each simulation takes place in a sub-band of 0.606814 Hz, centered at f_* . The injected signal binary parameters, $\{a_0, T_{\text{asc}}, P\}_{\text{inj}}$, correspond to their central values in Table I. For each simulation we generate two sets of atoms, the first set follows the proper motion of PSR J0437–4715 with $\alpha(t)$ and $\delta(t)$ varying according to (A1) and (A2), while the second set is fixed at the initial sky coordinates, with $\alpha(t) = \alpha$ and $\delta(t) = \delta$. We use the subscript PM to denote the former set of atoms and ZPM for the latter set. We summarize the result of the simulations in terms of the mean difference between log likelihoods per atom set. We find $\langle \mathcal{L}_{\text{ZPM}} - \mathcal{L}_{\text{PM}} \rangle = 0.13$ and $\langle \mathcal{L}_{\text{ZPM}} - \mathcal{L}_{\text{PM}} \rangle = 0.55$ for

$T_{\text{drift}}^{(\text{i})}$ and $T_{\text{drift}}^{(\text{ii})}$ respectively.

Given the small differences between maximum log likelihoods found above, we perform the search with $\alpha(t) = \alpha$ and $\delta(t) = \delta$ fixed in this paper instead of propagating according to (A1) and (A2). However, to be conservative, we reduce the thresholds per sub-band (See Section IV C) by 0.13 for $T_{\text{drift}}^{(\text{i})}$, and by 0.55 for $T_{\text{drift}}^{(\text{ii})}$.

$\Psi(t)$ is composed of four contributions: (i) the rotation of the star, (ii) Earth’s orbital motion around the SSB, (iii) Earth’s rotation, and (iv) the proper motion of the star. In this appendix we focus on contribution (iv), denoted by $\Psi_{\text{pm}}(t)$, which is given by Eq. (16) of Ref. [74], namely

$$\Psi_{\text{pm}}(t) = 2\pi \left[\frac{\mathbf{v}_{\perp} \cdot \mathbf{r}_{\text{ES}}(t)}{cD} \right] ft, \quad (\text{A3})$$

where $\mathbf{r}_{\text{ES}}(t)$ is the vector joining the SSB with the center of the Earth. The maximum number of cycles $\Psi_{\text{pm}}(t)$ contributes during the full observation of duration T_{obs} is calculated using PSR J0437–4715 values for $|\mathbf{v}_{\perp}| = 104.71 \pm 0.95$ km/s [38] and $D = 156.3 \pm 1.3$ pc [38], $|\mathbf{r}_{\text{ES}}(t)| = 1$ AU, $\max(f) = 500$ Hz, and $t = T_{\text{obs}}$ in Eq. (A3). This yields

$$\Psi_{\text{pm}}^{\text{max}}(T_{\text{obs}}) = 0.0342\pi, \quad (\text{A4})$$

which is well below the quarter-cycle criterion set in Appendix A of Ref. [74] to ignore a phase contribution. The loss in signal-to-noise ratio is quantified as $1 - \text{FF}$ where FF is the fitting factor that measures the offset between a signal and a filter (defined in Eq. (65) of Ref. [74]). For contribution (iv), we find

$$1 - \text{FF} \geq 1 - \frac{\sin(0.0342\pi)}{0.0342\pi} \approx 0.002, \quad (\text{A5})$$

that is, the loss in signal-to-noise ratio does not exceed 0.2%. We simplify the search by dropping $\Psi_{\text{pm}}(t)$ from $\Psi(t)$.

Appendix B: Shklovskii effect

The Shklovskii effect refers to the increase of the observed frequency derivative $|\dot{f}_{\star}^{(\text{obs})}|$ of a pulsar due to its proper motion [59]. Pulsars with high transverse velocities appear to accelerate in the reference frame of an Earth-bound observer. For PSR J0437–4715, this effect is considerable. Following Ref. [59] the kinetic correction due to the Shklovskii effect is given by

$$\dot{f}_{\text{K}} = -\frac{|\mathbf{v}_{\perp}|^2}{cD} f_{\star}, \quad (\text{B1})$$

where \dot{f}_{K} is the (kinetic) Shklovskii correction to \dot{f} . It is well known that the Shklovskii effect is significant in radio pulsar timing experiments targeting PSR J0437–4715, because its proper motion is relatively high, and it is located relatively near the Earth $D = 156.3 \pm 1.3$ pc [52, 75]. It is therefore natural to ask whether the Shklovskii effect is significant in GW searches too, e.g. when calculating the \mathcal{F} - and \mathcal{J} -statistics. We study this question in this appendix.

Following Appendix A of Ref. [50], the phase of the GW signal, in the rest frame of the NS, is given by

$$\Psi_{\star}(\tau) = \Phi_0 + 2\pi \sum_{k=0}^s f_{\star}^{(k)} \frac{\tau^{k+1}}{(k+1)!}, \quad (\text{B2})$$

where τ is the proper time in the NS rest frame, and $f_{\star}^{(k)}$ is the k th time derivative of $f_{\star}(t)$ evaluated at $\tau = 0$. The

NS is assumed to move at uniform velocity. Its position vector with respect to the origin of the SSB is given by

$$\mathbf{r}_{\star}(t) = D\mathbf{n}_0 + |\mathbf{v}_{\star}|\mathbf{n}_v \left(t + \frac{D}{c} \right), \quad (\text{B3})$$

with $\mathbf{n}_o = \mathbf{r}_{\star}(t)/|\mathbf{r}_{\star}(t)|$, $\mathbf{v}_{\star} = d\mathbf{r}_{\star}(t)/dt$, and $\mathbf{n}_v = \mathbf{v}_{\star}/v_{\star}$. The global time t in Eq. (B3) is the time coordinate in the SSB rest frame. Eq. (B3) excludes the binary orbit of the NS, because in this appendix we study the effect of proper motion on the \mathcal{F} -statistic for an isolated source. The binary orbit is included later, when constructing the \mathcal{J} -statistic from a linear, Jacobi-Anger combination of \mathcal{F} -statistic values. [35]

The wavefront recorded at the SSB at some time t is originally emitted at t' , with

$$t = t' + \frac{|\mathbf{r}_{\star}(t')|}{c}. \quad (\text{B4})$$

The time t' is related to τ through special relativistic time dilation,

$$\tau = \sqrt{1 - \beta_{\star}^2} \left(t' + \frac{D}{c} \right), \quad (\text{B5})$$

with $\beta_{\star} = |\mathbf{v}_{\star}|/c$. Eq. (B5) assumes $\tau = 0$, when the star is located at $\mathbf{r}_{\star} = D\mathbf{n}_0$. The GW signal phase at the SSB, $\Psi_{\text{SSB}}(t)$, takes the form (see Appendix A of [50])

$$\begin{aligned} \Psi_{\text{SSB}}(t) = & \Phi_0 + 2\pi \sum_{k=0}^s \frac{f_{\star}^{(k)}}{(k+1)!} (1 - \beta_{\star}^2)^{(k+1)/2} \times \\ & \times \left[t'(t) + \frac{D}{c} \right]^{k+1}, \end{aligned} \quad (\text{B6})$$

where $t'(t)$ is the solution of the implicit equation (B4) for t fixed:

$$\begin{aligned} t' = & \frac{1}{1 - \beta_{\star}^2} \left\{ t + \frac{D}{c} \beta_{\star} [\beta_{\star} + \mathbf{n}_0 \cdot \mathbf{n}_v] \right. \\ & - \left[\beta_{\star}^2 t^2 + 2 \frac{D}{c} \beta_{\star}^2 (\beta_{\star} + \mathbf{n}_0 \cdot \mathbf{n}_v) t \right. \\ & \left. \left. + \frac{D^2}{c^2} (1 + \beta_{\star} \mathbf{n}_0 \cdot \mathbf{n}_v) \right]^{1/2} \right\}. \end{aligned} \quad (\text{B7})$$

Upon Taylor expanding $\Psi_{\text{SSB}}(t)$ around $t = 0$ to quadratic order, using Eqs. (B6) and (B7), we find

$$\begin{aligned} \frac{\Psi_{\text{SSB}} - \Phi_0}{2\pi} = & f_{\text{SSB}}^{(0)} t \\ & + \left\{ f_{\text{SSB}}^{(1)} + \frac{[(\mathbf{n}_0 \cdot \mathbf{n}_v)^2 - 1] \beta_{\star}^2}{(1 + \beta_{\star} \mathbf{n}_0 \cdot \mathbf{n}_v)^2 (D/c)} f_{\text{SSB}}^{(0)} \right\} \frac{t^2}{2} \\ & + \mathcal{O}(t^3), \end{aligned} \quad (\text{B8})$$

where

$$f_{\text{SSB}}^{(k)} = \frac{(1 - \beta_\star^2)^{(k+1)/2}}{(1 + \beta_\star \mathbf{n}_0 \cdot \mathbf{n}_v)^{k+1}} f_\star^{(k)} \quad (\text{B9})$$

is the Doppler corrected frequency ($k = 0$) or its derivatives ($k > 0$), as measured in the SSB frame. The reader is directed to Eq. (119) in Ref. [50] for the complete Taylor expansion of $\Psi_{\text{SSB}}(t)$.

The first term in square brackets in Eq. (B8) equals the frequency derivative observed in the SSB, i.e. $f_{\text{SSB}}^{(1)} = \dot{f}_\star^{(\text{obs})}$. The second term,

$$\Delta f_{\text{SSB}}^{(1)} = \frac{[(\mathbf{n}_0 \cdot \mathbf{n}_v)^2 - 1] \beta_\star^2}{(1 + \beta_\star \mathbf{n}_0 \cdot \mathbf{n}_v)^2 (D/c)} f_{\text{SSB}}^{(0)}, \quad (\text{B10})$$

is a correction proportional to f_\star as observed at the SSB. In PSR J0437–4715, one has $\beta_\star \approx 3.5 \times 10^{-4} \ll 1$, which justifies the Taylor expansion

$$\Delta f_{\text{SSB}}^{(1)} \approx -\frac{c[1 - (\mathbf{n}_0 \cdot \mathbf{n}_v)^2] f_{\text{SSB}}^{(0)}}{D} \beta_\star^2 + \mathcal{O}(\beta_\star^3). \quad (\text{B11})$$

Writing the transverse velocity as $\mathbf{v}_\perp = \mathbf{v}_\star - (\mathbf{n}_0 \cdot \mathbf{v}_\star) \mathbf{n}_0$, one can rewrite Eq. (B11) as

$$\Delta f_{\text{SSB}}^{(1)} \approx -\frac{|\mathbf{v}_\perp|^2}{cD} f_{\text{SSB}}^{(0)} + \mathcal{O}(\beta_\star^3), \quad (\text{B12})$$

Eq. (B12) is identical to the Shklovskii effect in Eq. (B1).

When calculating the \mathcal{F} -statistic and hence the \mathcal{J} -statistic, the phase of the GW signal as measured in Earth’s reference frame, i.e. Eq. (130) in Ref. [50], is written in terms of the spin-down parameters $f_0^{(k)}$. The latter quantities do not equal $f_{\text{SSB}}^{(k)}$ (defined by Eq. (B9)). Instead they equal the terms in Eq. (B8) proportional to t^k , for example

$$f_0^{(0)} = f_{\text{SSB}}^{(0)}, \quad (\text{B13})$$

$$f_0^{(1)} = f_{\text{SSB}}^{(1)} + \Delta f_{\text{SSB}}^{(1)}, \quad (\text{B14})$$

and so forth. From Eq. (B12), Eq. (B14), and $f_{\text{SSB}}^{(1)} = \dot{f}_\star^{(\text{obs})}$, it is clear that the first spin-down parameter $f_0^{(1)}$ entering the calculation of the \mathcal{F} -statistic (and hence \mathcal{J} -statistic) is given by

$$f_0^{(1)} = \dot{f}_\star^{(\text{obs})} + \dot{f}_K. \quad (\text{B15})$$

That is, the Shklovskii effect enters *naturally* into the calculation of the \mathcal{F} - and \mathcal{J} -statistics, as laid out in Ref. [50] and implemented in the LALSuite. This exercise can be extended to higher-order frequency derivatives.

TABLE V. Terminating frequency bin, $q^*(t_{N_T})$, log likelihood, $\max(\mathcal{L})$, detection threshold, \mathcal{L}_{th} , and time of ascension, T_{asc} , of the surviving candidates. All candidates share the same template for a_0 and P , given by the central values in Table I.

$q^*(t_{N_T})$ (Hz)	$\max(\mathcal{L})$	\mathcal{L}_{th}	T_{asc} (GPS time)
219.6208803	148.23	148.22	1265652983.7837
248.7994215	150.25	150.24	1265652985.7228
271.3585692	153.38	153.37	1265653034.7963
320.2733869	154.31	154.30	1265652922.2337
371.4158598	153.82	153.82	1265652985.7228

Appendix C: Surviving candidates and follow-up

In this appendix we show how varying the sky position of the surviving candidates, listed in Table V, affects \mathcal{L} . In general an astrophysical candidate’s \mathcal{L} should diminish, as one points away from its original position. Moreover the contours of $\mathcal{L}(\alpha, \delta)$ should be elliptical, with the orientation of their major axis changing with sky location. Similar tests have been done in previous works, such as in Appendix B.1 of [45] and in Ref. [73]. Figure 3 presents the results of the additional follow-up in terms of sky maps and cross-sections of constant- δ and constant- α .

The sky maps in the left panels of Figure 3 cover a 0.48×0.48 arcmin² patch of sky centered at the source location. The image uses $51 \times 51 = 2601$ evenly spaced grid points. The color of a pixel represents the value of the normalized log likelihood, i.e. $\rho = \mathcal{L}/\max(\mathcal{L})$, obtained in that pixel. In general the contours of $\mathcal{L}(\alpha, \delta)$ for an injection (analogous to the point spread function of an electromagnetic telescope) are elliptical, centered at the source, with orientation and eccentricity depending on α , δ , and the orientation of the source [45]. None of the ellipses are centered at the source location¹. The closest ones, with centroid offsets $\Delta\alpha = 0.006$ arcsec and $\Delta\delta = 0$ arcsec and $\Delta\alpha = -0.012$ arcsec and $\Delta\delta = 0$ arcsec, are associated with the 248.58 Hz sub-band and 371.15 Hz sub-band candidates, respectively, which happen to share the same T_{asc} . All other ellipses are off-center by more than 1 arcsec. None of the ellipses are centered exactly at the source location even when accounting for PSR J0437–4715’s proper motion, i.e. $\Delta\alpha = 0.12$ arcsec and $\Delta\delta = -0.071$ arcsec.

Constant- δ and constant- α cross-sections are graphed in the central and right panels of Figure 3 respectively. The maximum offset is 0.24 arcmin and uses 50 evenly spaced trials to resolve the rapid change of \mathcal{L} . The coordinate offset is graphed on the horizontal axis while ρ is plotted on the vertical axis. The black dashed line, in both panels, represent the normalized candidate thresh-

¹ The center of the ellipse is calculated by averaging the position of pixels satisfying $\mathcal{L} > \mathcal{L}_{\text{th}}$ (marked by red dots in Figure 2).

old $\mathcal{L}_{\text{th}}/\max(\mathcal{L})$. Only the 371.15 Hz sub-band candidate shows a monotonic decrease in ρ , as both the δ and α offsets increase, although ρ falls away non-monotonically in every sub-band. The graphs settle around $\rho \approx 0.8$ which is consistent with noise-only \mathcal{L} values.

For completeness, Figure 4 shows the optimal path relative to the starting frequency bin, $q^*(t_0)$, for the five $T_{\text{drift}}^{(\text{ii})}$ survivors as a function of the search epoch. There is no clear trend among the optimal paths. In particular

the two paths for the candidates sharing the same T_{asc} , viz. 248.58 Hz and 371.15 Hz, seem to be unrelated.

Given that the number of surviving candidates is consistent with the number of expected false alarms, and that all five are near \mathcal{L}_{th} , we leave further investigations into their origin until newer data sets and/or more sensitive pipelines become available, starting with the fourth LIGO-Virgo-KAGRA observing run.

-
- [1] K. Riles, Gravitational waves: Sources, detectors and searches, *Progress in Particle and Nuclear Physics* **68**, 1 (2013), [arXiv:1209.0667 \[hep-ex\]](#).
- [2] G. M. Harry and LIGO Scientific Collaboration, Advanced LIGO: the next generation of gravitational wave detectors, *Classical and Quantum Gravity* **27**, 084006 (2010).
- [3] LIGO Scientific Collaboration, J. Aasi, B. P. Abbott, R. Abbott, T. Abbott, M. R. Abernathy, K. Ackley, C. Adams, T. Adams, P. Addesso, and et al., Advanced LIGO, *Classical and Quantum Gravity* **32**, 074001 (2015), [arXiv:1411.4547 \[gr-qc\]](#).
- [4] N. Andersson, V. Ferrari, D. I. Jones, K. D. Kokkotas, B. Krishnan, J. S. Read, L. Rezzolla, and B. Zink, Gravitational waves from neutron stars: promises and challenges, *General Relativity and Gravitation* **43**, 409 (2011), [arXiv:0912.0384 \[astro-ph.SR\]](#).
- [5] F. Acernese, M. Agathos, K. Agatsuma, D. Aisa, N. Allemandou, A. Allocca, J. Amarni, P. Astone, G. Balestri, G. Ballardin, and et al., Advanced Virgo: a second-generation interferometric gravitational wave detector, *Classical and Quantum Gravity* **32**, 024001 (2015), [arXiv:1408.3978 \[gr-qc\]](#).
- [6] T. Akutsu, M. Ando, K. Arai, Y. Arai, S. Araki, A. Araya, N. Aritomi, Y. Aso, S. Bae, Y. Bae, and et al., Overview of KAGRA: Detector design and construction history, *Progress of Theoretical and Experimental Physics* **2021**, 05A101 (2021), [arXiv:2005.05574 \[physics.ins-det\]](#).
- [7] G. Ushomirsky, C. Cutler, and L. Bildsten, Deformations of accreting neutron star crusts and gravitational wave emission, *MNRAS* **319**, 902 (2000), [arXiv:astro-ph/0001136 \[astro-ph\]](#).
- [8] N. K. Johnson-McDaniel and B. J. Owen, Maximum elastic deformations of relativistic stars, *Phys. Rev. D* **88**, 044004 (2013), [arXiv:1208.5227 \[astro-ph.SR\]](#).
- [9] C. Cutler, Gravitational waves from neutron stars with large toroidal B fields, *Phys. Rev. D* **66**, 084025 (2002), [arXiv:gr-qc/0206051 \[gr-qc\]](#).
- [10] A. Mastrano, A. Melatos, A. Reisenegger, and T. Akgün, Gravitational wave emission from a magnetically deformed non-barotropic neutron star, *MNRAS* **417**, 2288 (2011), [arXiv:1108.0219 \[astro-ph.HE\]](#).
- [11] P. D. Lasky and A. Melatos, Tilted torus magnetic fields in neutron stars and their gravitational wave signatures, *Phys. Rev. D* **88**, 103005 (2013), [arXiv:1310.7633 \[astro-ph.HE\]](#).
- [12] J. S. Heyl, Low-Mass X-Ray Binaries May Be Important Laser Interferometer Gravitational-Wave Observational Sources After All, *ApJ* **574**, L57 (2002).
- [13] P. Arras, E. E. Flanagan, S. M. Morsink, A. K. Schenk, S. A. Teukolsky, and I. Wasserman, Saturation of the r-Mode Instability, *ApJ* **591**, 1129 (2003), [arXiv:astro-ph/0202345 \[astro-ph\]](#).
- [14] R. Bondarescu, S. A. Teukolsky, and I. Wasserman, Spinning down newborn neutron stars: Nonlinear development of the r-mode instability, *Phys. Rev. D* **79**, 104003 (2009), [arXiv:0809.3448 \[astro-ph\]](#).
- [15] C. Peralta, A. Melatos, M. Giacobello, and A. Ooi, Gravitational Radiation from Nonaxisymmetric Spherical Couette Flow in a Neutron Star, *ApJ* **644**, L53 (2006), [arXiv:gr-qc/0604123 \[gr-qc\]](#).
- [16] C. A. van Eysden and A. Melatos, Gravitational radiation from pulsar glitches, *Classical and Quantum Gravity* **25**, 225020 (2008), [arXiv:0809.4352 \[gr-qc\]](#).
- [17] M. F. Bennett, C. A. van Eysden, and A. Melatos, Continuous-wave gravitational radiation from pulsar glitch recovery, *MNRAS* **409**, 1705 (2010), [arXiv:1008.0236 \[astro-ph.SR\]](#).
- [18] A. Melatos, J. A. Douglass, and T. P. Simula, Persistent Gravitational Radiation from Glitching Pulsars, *ApJ* **807**, 132 (2015).
- [19] S. Johnston, D. R. Lorimer, P. A. Harrison, M. Bailes, A. G. Lynet, J. F. Bell, V. M. Kaspi, R. N. Manchester, N. D’Amico, L. Nleastrol, and et al., Discovery of a very bright, nearby binary millisecond pulsar, *Nature* **361**, 613 (1993).
- [20] V. Sosa Fiscella, S. del Palacio, L. Combi, C. O. Lousto, J. A. Combi, G. Gancio, F. García, E. Gutiérrez, F. Hauscarriaga, P. Kornecki, and et al., PSR J0437-4715: The Argentine Institute of Radioastronomy 2019-2020 Observational Campaign, *ApJ* **908**, 158 (2021), [arXiv:2010.00010 \[astro-ph.GA\]](#).
- [21] P. Haensel and J. L. Zdunik, Non-equilibrium processes in the crust of an accreting neutron star, *A&A* **227**, 431 (1990).
- [22] A. Melatos and D. J. B. Payne, Gravitational Radiation from an Accreting Millisecond Pulsar with a Magnetically Confined Mountain, *ApJ* **623**, 1044 (2005), [arXiv:astro-ph/0503287 \[astro-ph\]](#).
- [23] K. Wette, M. Vigelius, and A. Melatos, Sinking of a magnetically confined mountain on an accreting neutron star, *MNRAS* **402**, 1099 (2010), [arXiv:0910.5064 \[astro-ph.HE\]](#).
- [24] N. Andersson, K. D. Kokkotas, and N. Stergioulas, On the Relevance of the R-Mode Instability for Accreting Neutron Stars and White Dwarfs, *ApJ* **516**, 307 (1999), [arXiv:astro-ph/9806089 \[astro-ph\]](#).

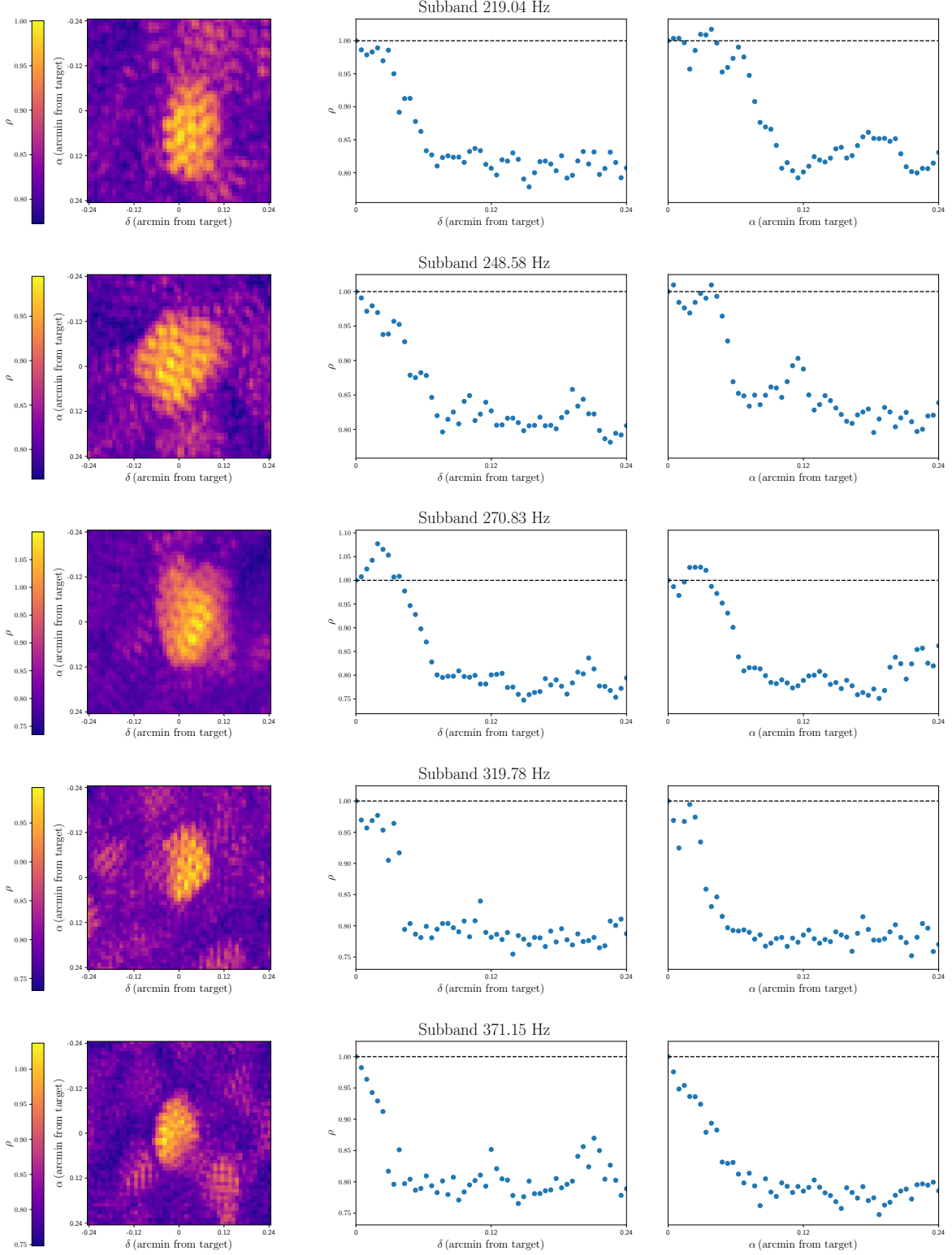


FIG. 3. Sky maps of $\rho(\alpha, \delta) = \mathcal{L}(\alpha, \delta)/\max(\mathcal{L})$ (left panel), and slices of ρ at constant α (central panel) and constant δ (right panel) for the five $T_{\text{drift}}^{(ii)}$ survivors. The sky maps consist of 2601 regularly spaced sky locations, with each location colored by its ρ value, spanning a sky area of 0.23 arcmin^2 centered around the source position. For both the central and right panels, ρ is plotted on the vertical axis, while the dashed black line represents the normalized candidate threshold, i.e. $\mathcal{L}_{\text{th}}/\max(\mathcal{L})$.

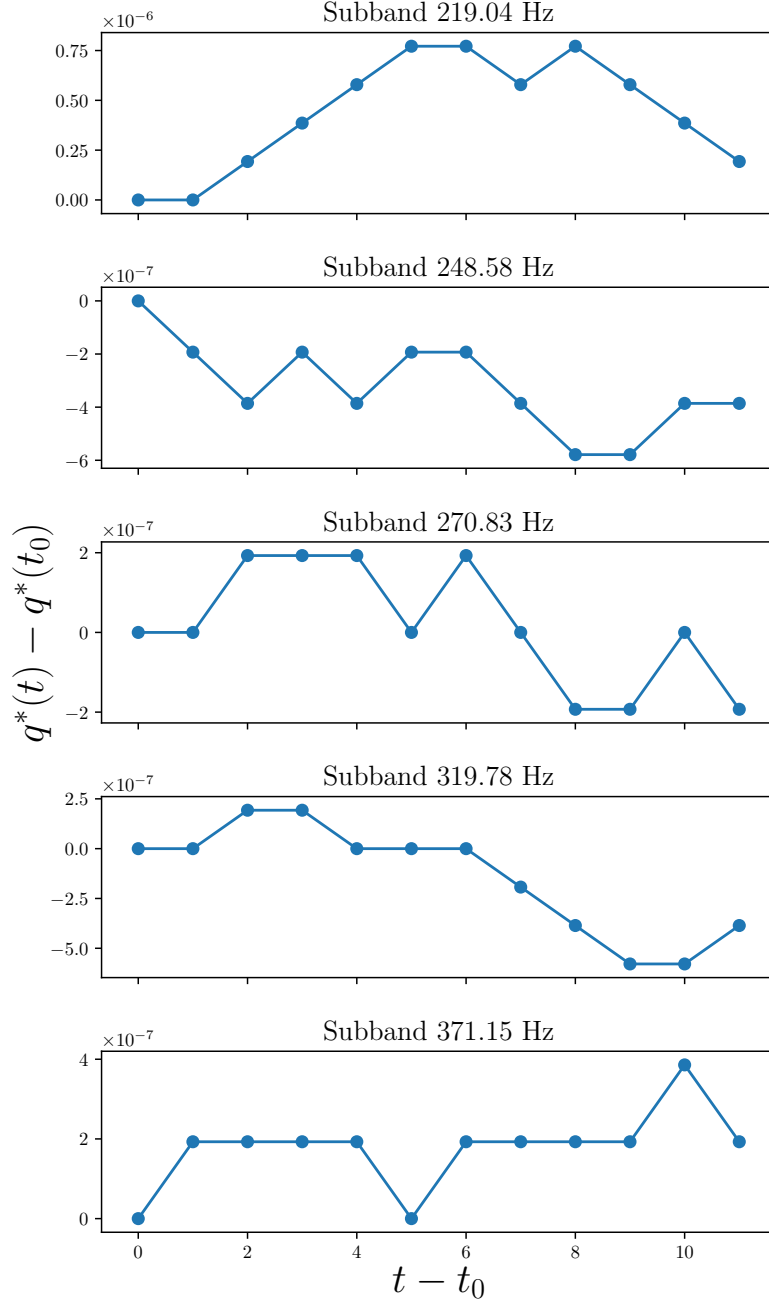


FIG. 4. Optimal path for the five $T_{\text{drift}}^{(ii)}$ survivors, measured from the starting frequency bin $q^*(t_0)$, as a function of epoch t (in units of $T_{\text{drift}}^{(ii)} = 30$ days).

- [25] N. Andersson, K. Kokkotas, and B. F. Schutz, Gravitational Radiation Limit on the Spin of Young Neutron Stars, *ApJ* **510**, 846 (1999), [arXiv:astro-ph/9805225 \[astro-ph\]](#).
- [26] L. Bildsten, Gravitational Radiation and Rotation of Accreting Neutron Stars, *ApJ* **501**, L89 (1998), [arXiv:astro-ph/9804325 \[astro-ph\]](#).
- [27] Y. Levin, Runaway Heating by R-Modes of Neutron Stars in Low-Mass X-Ray Binaries, *ApJ* **517**, 328 (1999), [arXiv:astro-ph/9810471 \[astro-ph\]](#).
- [28] M. Nayyar and B. J. Owen, R-modes of accreting hyperon stars as persistent sources of gravitational waves, *Phys. Rev. D* **73**, 084001 (2006), [arXiv:astro-ph/0512041 \[astro-ph\]](#).
- [29] S. D. Mohanty, I. S. Heng, D. G. Blair, S. V. Dhurandhar, M. Tobar, and E. Ivanov, A data analysis approach for detecting gravitational waves from PSR 0437-4715, *MNRAS* **301**, 469 (1998).
- [30] B. P. Abbott, R. Abbott, T. D. Abbott, S. Abraham, F. Acernese, K. Ackley, C. Adams, R. X. Adhikari, V. B.

- Adya, C. Affeldt, and et al., Searches for Gravitational Waves from Known Pulsars at Two Harmonics in 2015-2017 LIGO Data, *ApJ* **879**, 10 (2019), [arXiv:1902.08507 \[astro-ph.HE\]](#).
- [31] R. Abbott, T. D. Abbott, S. Abraham, F. Acernese, K. Ackley, A. Adams, C. Adams, R. X. Adhikari, V. B. Adya, C. Affeldt, and et al., Gravitational-wave Constraints on the Equatorial Ellipticity of Millisecond Pulsars, *ApJ* **902**, L21 (2020), [arXiv:2007.14251 \[astro-ph.HE\]](#).
- [32] The LIGO Scientific Collaboration, the Virgo Collaboration, the KAGRA Collaboration, R. Abbott, H. Abe, F. Acernese, K. Ackley, N. Adhikari, R. X. Adhikari, V. K. Adkins, and et al., Searches for Gravitational Waves from Known Pulsars at Two Harmonics in the Second and Third LIGO-Virgo Observing Runs, arXiv e-prints , [arXiv:2111.13106 \(2021\)](#), [arXiv:2111.13106 \[astro-ph.HE\]](#).
- [33] S. Suvorova, L. Sun, A. Melatos, W. Moran, and R. J. Evans, Hidden Markov model tracking of continuous gravitational waves from a neutron star with wandering spin, *Phys. Rev. D* **93**, 123009 (2016), [arXiv:1606.02412 \[astro-ph.IM\]](#).
- [34] B. P. Abbott, R. Abbott, T. D. Abbott, F. Acernese, K. Ackley, C. Adams, T. Adams, P. Addesso, R. X. Adhikari, V. B. Adya, and et al., Search for gravitational waves from Scorpius X-1 in the first Advanced LIGO observing run with a hidden Markov model, *Phys. Rev. D* **95**, 122003 (2017), [arXiv:1704.03719 \[gr-qc\]](#).
- [35] S. Suvorova, P. Clearwater, A. Melatos, L. Sun, W. Moran, and R. J. Evans, Hidden Markov model tracking of continuous gravitational waves from a binary neutron star with wandering spin. II. Binary orbital phase tracking, *Phys. Rev. D* **96**, 102006 (2017), [arXiv:1710.07092 \[astro-ph.IM\]](#).
- [36] B. P. Abbott, R. Abbott, T. D. Abbott, S. Abraham, F. Acernese, K. Ackley, C. Adams, R. X. Adhikari, V. B. Adya, C. Affeldt, and et al., Search for gravitational waves from Scorpius X-1 in the second Advanced LIGO observing run with an improved hidden Markov model, *Phys. Rev. D* **100**, 122002 (2019), [arXiv:1906.12040 \[gr-qc\]](#).
- [37] The LIGO Scientific Collaboration, the Virgo Collaboration, the KAGRA Collaboration, R. Abbott, H. Abe, F. Acernese, K. Ackley, N. Adhikari, R. X. Adhikari, V. K. Adkins, and et al., Search for gravitational waves from Scorpius X-1 with a hidden Markov model in O3 LIGO data, arXiv e-prints , [arXiv:2201.10104 \(2022\)](#), [arXiv:2201.10104 \[gr-qc\]](#).
- [38] A. T. Deller, J. P. W. Verbiest, S. J. Tingay, and M. Bailes, Extremely High Precision VLBI Astrometry of PSR J0437-4715 and Implications for Theories of Gravity, *ApJ* **685**, L67 (2008), [arXiv:0808.1594 \[astro-ph\]](#).
- [39] S. Caride, R. Inta, B. J. Owen, and B. Rajbhandari, How to search for gravitational waves from r -modes of known pulsars, *Phys. Rev. D* **100**, 064013 (2019), [arXiv:1907.04946 \[gr-qc\]](#).
- [40] P. B. Covas, A. Effler, E. Goetz, P. M. Meyers, A. Neunzert, M. Oliver, B. L. Pearlstone, V. J. Roma, R. M. S. Schofield, V. B. Adya, and et al., Identification and mitigation of narrow spectral artifacts that degrade searches for persistent gravitational waves in the first two observing runs of Advanced LIGO, *Phys. Rev. D* **97**, 082002 (2018), [arXiv:1801.07204 \[astro-ph.IM\]](#).
- [41] B. B. P. Perera, M. E. DeCesar, P. B. Demorest, M. Kerr, L. Lentati, D. J. Nice, S. Osłowski, S. M. Ransom, M. J. Keith, Z. Arzoumanian, and et al., The International Pulsar Timing Array: second data release, *MNRAS* **490**, 4666 (2019), [arXiv:1909.04534 \[astro-ph.HE\]](#).
- [42] A. Mukherjee, C. Messenger, and K. Riles, Accretion-induced spin-wandering effects on the neutron star in Scorpius X-1: Implications for continuous gravitational wave searches, *Phys. Rev. D* **97**, 043016 (2018), [arXiv:1710.06185 \[gr-qc\]](#).
- [43] H. Middleton, P. Clearwater, A. Melatos, and L. Dunn, Search for gravitational waves from five low mass x-ray binaries in the second Advanced LIGO observing run with an improved hidden Markov model, *Phys. Rev. D* **102**, 023006 (2020), [arXiv:2006.06907 \[astro-ph.HE\]](#).
- [44] D. Beniwal, P. Clearwater, L. Dunn, A. Melatos, and D. Ottaway, Search for continuous gravitational waves from ten H.E.S.S. sources using a hidden Markov model, *Phys. Rev. D* **103**, 083009 (2021), [arXiv:2102.06334 \[astro-ph.HE\]](#).
- [45] The LIGO Scientific Collaboration, the Virgo Collaboration, the KAGRA Collaboration, R. Abbott, T. D. Abbott, F. Acernese, K. Ackley, C. Adams, N. Adhikari, R. X. Adhikari, and et al., Search for continuous gravitational waves from 20 accreting millisecond X-ray pulsars in O3 LIGO data, arXiv e-prints , [arXiv:2109.09255 \(2021\)](#), [arXiv:2109.09255 \[astro-ph.HE\]](#).
- [46] A. Idrisy, B. J. Owen, and D. I. Jones, R -mode frequencies of slowly rotating relativistic neutron stars with realistic equations of state, *Phys. Rev. D* **91**, 024001 (2015), [arXiv:1410.7360 \[gr-qc\]](#).
- [47] B. G. Quinn and E. J. Hannan, *The estimation and tracking of frequency* (Cambridge University Press, United Kingdom, 2001).
- [48] C. Messenger, H. J. Bulten, S. G. Crowder, V. Dergachev, D. K. Galloway, E. Goetz, R. J. G. Jonker, P. D. Lasky, G. D. Meadors, A. Melatos, and et al., Gravitational waves from Scorpius X-1: A comparison of search methods and prospects for detection with advanced detectors, *Phys. Rev. D* **92**, 023006 (2015), [arXiv:1504.05889 \[gr-qc\]](#).
- [49] A. Viterbi, Error bounds for convolutional codes and an asymptotically optimum decoding algorithm, *IEEE Transactions on Information Theory* **13**, 260 (1967).
- [50] P. Jaranowski, A. Królak, and B. F. Schutz, Data analysis of gravitational-wave signals from spinning neutron stars: The signal and its detection, *Phys. Rev. D* **58**, 063001 (1998), [arXiv:gr-qc/9804014 \[gr-qc\]](#).
- [51] R. Prix and B. Krishnan, Targeted search for continuous gravitational waves: Bayesian versus maximum-likelihood statistics, *Classical and Quantum Gravity* **26**, 204013 (2009), [arXiv:0907.2569 \[gr-qc\]](#).
- [52] J. P. W. Verbiest, M. Bailes, W. van Straten, G. B. Hobbs, R. T. Edwards, R. N. Manchester, N. D. R. Bhat, J. M. Sarkissian, B. A. Jacoby, and S. R. Kulkarni, Precision Timing of PSR J0437-4715: An Accurate Pulsar Distance, a High Pulsar Mass, and a Limit on the Variation of Newton's Gravitational Constant, *ApJ* **679**, 675 (2008), [arXiv:0801.2589 \[astro-ph\]](#).
- [53] R. Prix, LIGO Report T0900149 (June 2011).
- [54] M. Durant, O. Kargaltsev, G. G. Pavlov, P. M. Kowalski, B. Posselt, M. H. van Kerkwijk, and D. L. Kaplan, The Spectrum of the Recycled PSR J0437-4715 and Its White Dwarf Companion, *ApJ* **746**, 6 (2012), [arXiv:1111.2346](#)

- [astro-ph.HE].
- [55] J. F. Bell, M. Bailes, and M. S. Bessell, Optical detection of the companion of the millisecond pulsar J0437-4715, *Nature* **364**, 603 (1993).
- [56] V. E. Zavlin, G. G. Pavlov, D. Sanwal, R. N. Manchester, J. Trümper, J. P. Halpern, and W. Becker, X-Radiation from the Millisecond Pulsar J0437-4715, *ApJ* **569**, 894 (2002), [arXiv:astro-ph/0112544 \[astro-ph\]](#).
- [57] O. Kargaltsev, G. G. Pavlov, and R. W. Romani, Ultraviolet Emission from the Millisecond Pulsar J0437-4715, *ApJ* **602**, 327 (2004), [arXiv:astro-ph/0310854 \[astro-ph\]](#).
- [58] M. Sieniawska and D. I. Jones, Gravitational waves from spinning neutron stars as not-quite-standard sirens, *MNRAS* **509**, 5179 (2022), [arXiv:2108.11710 \[astro-ph.HE\]](#).
- [59] I. S. Shklovskii, Possible Causes of the Secular Increase in Pulsar Periods., *Soviet Ast.* **13**, 562 (1970).
- [60] LIGO Scientific Collaboration, *LIGO Algorithm Library - LALSuite*, free software (GPL) (2018).
- [61] J. M. Cordes and D. J. Helfand, Pulsar timing .III. Timing noise of 50 pulsars., *ApJ* **239**, 640 (1980).
- [62] J. M. Cordes and G. Greenstein, Pulsar timing .IV. Physical models for timing noise processes., *ApJ* **245**, 1060 (1981).
- [63] M. A. Alpar, K. S. Cheng, D. Pines, and J. Shaham, The large glitch from PSR 0355+54 and its post-glitch relaxation., *MNRAS* **233**, 25 (1988).
- [64] S. Price, B. Link, S. N. Shore, and D. J. Nice, Time-correlated structure in spin fluctuations in pulsars, *MNRAS* **426**, 2507 (2012), [arXiv:1208.0807 \[astro-ph.HE\]](#).
- [65] A. G. Lyne, S. L. Shemar, and F. G. Smith, Statistical studies of pulsar glitches, *MNRAS* **315**, 534 (2000).
- [66] P. M. McCulloch, P. A. Hamilton, D. McConnell, and E. A. King, The Vela glitch of Christmas 1988, *Nature* **346**, 822 (1990).
- [67] T. Wong, D. C. Backer, and A. G. Lyne, Observations of a Series of Six Recent Glitches in the Crab Pulsar, *ApJ* **548**, 447 (2001), [arXiv:astro-ph/0010010 \[astro-ph\]](#).
- [68] P. Leaci and R. Prix, Directed searches for continuous gravitational waves from binary systems: Parameter-space metrics and optimal Scorpius X-1 sensitivity, *Phys. Rev. D* **91**, 102003 (2015), [arXiv:1502.00914 \[gr-qc\]](#).
- [69] D. Davis, J. S. Areeda, B. K. Berger, R. Bruntz, A. Effler, R. C. Essick, R. P. Fisher, P. Godwin, E. Goetz, A. F. Hellmich-Cornell, and et al., LIGO detector characterization in the second and third observing runs, *Classical and Quantum Gravity* **38**, 135014 (2021), [arXiv:2101.11673 \[astro-ph.IM\]](#).
- [70] J. Zweizig and K. Riles, LIGO-T2000384-v4: Information on self-gating of h(t) used in O3 continuous-wave and stochastic searches.
- [71] G. Vajente, Y. Huang, M. Isi, J. C. Driggers, J. S. Kissel, M. J. Szczepańczyk, and S. Vitale, Machine-learning nonstationary noise out of gravitational-wave detectors, *Phys. Rev. D* **101**, 042003 (2020), [arXiv:1911.09083 \[gr-qc\]](#).
- [72] E. Goetz, A. Neunzert, K. Riles, A. Matas, S. Kandhasamy, J. Tasson, C. Barschaw, H. Middleton, S. Hughey, L. Mueller, J. Heinzl, J. Carlin, A. Vargas, and I. Hollows, T2100200-v1: O3 lines and combs in found in self-gated C01 data.
- [73] D. Jones, L. Sun, J. Carlin, L. Dunn, M. Millhouse, H. Middleton, P. Meyers, P. Clearwater, D. Beniwal, L. Strang, and et al., Validating continuous gravitational-wave candidates based on Doppler modulation, *arXiv e-prints*, [arXiv:2203.14468 \(2022\)](#), [arXiv:2203.14468 \[gr-qc\]](#).
- [74] P. Jaranowski and A. Królak, Data analysis of gravitational-wave signals from spinning neutron stars. II. Accuracy of estimation of parameters, *Phys. Rev. D* **59**, 063003 (1999), [arXiv:gr-qc/9809046 \[gr-qc\]](#).
- [75] J. F. Bell, M. Bailes, R. N. Manchester, J. M. Weisberg, and A. G. Lyne, The Proper Motion and Wind Nebula of the Nearby Millisecond Pulsar J0437-4715, *ApJ* **440**, L81 (1995).
- [76] W. van Straten, M. Bailes, M. Britton, S. R. Kulkarni, S. B. Anderson, R. N. Manchester, and J. Sarkissian, A test of general relativity from the three-dimensional orbital geometry of a binary pulsar, *Nature* **412**, 158 (2001), [arXiv:astro-ph/0108254 \[astro-ph\]](#).
- [77] Kagra Collaboration, T. Akutsu, M. Ando, K. Arai, Y. Arai, S. Araki, A. Araya, N. Aritomi, H. Asada, Y. Aso, and et al., KAGRA: 2.5 generation interferometric gravitational wave detector, *Nature Astronomy* **3**, 35 (2019), [arXiv:1811.08079 \[gr-qc\]](#).